

Optomechanical response with nanometer resolution in the self-mixing signal of a terahertz quantum cascade laser

Andrea Ottomaniello,^{1,2} James Keeley,³ Pierluigi Rubino,³ Lianhe Li,³ Marco Cecchini,² Edmund H. Linfield,³ A. Giles Davies,³ Paul Dean,³ Alessandro Pitanti,² and Alessandro Tredicucci^{1,2}

¹*Dipartimento di Fisica "E. Fermi", Università degli studi di Pisa, 56127 Pisa, Italy*

²*NEST, CNR -Istituto Nanoscienze and Scuola Normale Superiore, Piazza San Silvestro 12, 56127 Pisa, Italy*

³*Italy*

³*School of Electronic and Electrical Engineering, University of Leeds, Leeds LS29JT, United Kingdom*

(Dated: 13 July 2021)

The effectiveness of self-mixing interferometry has been demonstrated across the electromagnetic spectrum, from visible to microwave frequencies, in a plethora of sensing applications, ranging from distance measurement to material analysis, microscopy and coherent imaging. Owing to their intrinsic stability to optical feedback, quantum cascade lasers (QCLs) represent a source that offers unique and versatile characteristics to further improve the self-mixing functionality at mid-infrared and terahertz (THz) frequencies. Here, we show the feasibility of detecting with nanometer precision deeply subwavelength ($< \lambda/6000$) mechanical vibrations of a suspended Si_3N_4 -membrane used as the external element of a THz QCL feedback interferometric apparatus. Besides representing a platform for the characterization of small displacements, our self-mixing configuration can be exploited for the realization of optomechanical systems, where several laser sources can be linked together through a common mechanical microresonator actuated by radiation pressure.

The self-mixing (SM) effect describes the mixing of the intracavity electromagnetic field of a laser with its emitted radiation partially reinjected into the laser cavity¹. Although such optical feedback (OF) can be detrimental to laser operation², the SM effect can also be exploited for metrological applications³, through a technique known as laser-feedback interferometry (LFI)⁴. This homodyne technique, in which the laser acts simultaneously as source, mixer and shot-noise limited detector, allows retrieval of information about the external cavity, comprising the target and the external medium, by monitoring the response of the laser to OF. Thanks to the universal and simple character of the SM phenomenon, its functionality has been demonstrated from the visible to the microwave range using laser systems as diverse as gas lasers⁵, solid-state lasers⁶ and semiconductor lasers⁷. This has led to the development of a large number of sensing applications^{8,9} ranging from displacement measurement¹⁰ to material analysis¹¹, laser emission spectrometry¹² and coherent imaging^{13,14}. Among all kinds of semiconductor lasers, quantum cascade lasers (QCLs) allow further simplification of the SM scheme thanks to their intrinsic voltage sensitivity to OF. This allows the SM modulation to be measured directly, and with high sensitivity¹⁵, via the voltage variation across the active region with no need for an external photodetector¹⁶. Moreover, QCLs exhibit peculiar ultra-stability to OF¹⁷, due to their small linewidth enhancement factor¹⁸ ($0 < |\alpha| < 1$) and long photon to carrier lifetime ratio. These unique and versatile characteristics offer an opportunity for the development of high performance LFI schemes operating at mid-infrared and terahertz (THz) frequencies, for coherent imaging¹⁹ and displacement sensing^{20,21}. In fact, despite the relatively long wavelength, nanometer target displacements as low as $\lambda/100$ have been measured by adding a fast moving etalon in the external cavity²².

nanometer displacement sensing by showing the detection of deeply subwavelength vibrations ($< \lambda/6000$) of a suspended mechanical resonator, by employing a 3.34 THz QCL operating in continuous-wave (CW). The experimental results have been validated by solving the Lang-Kobayashi (LK) model²³ in the steady-state regime after calibration of the absolute membrane position. Furthermore, the measured oscillation amplitudes are shown to be in agreement with independent measurements performed using a laser Doppler vibrometer (LVD) operating in the visible region.

We chose as an external element a Si_3N_4 trampoline membrane, which is an optimum candidate for interferometric readout and optomechanical applications^{24,25}. Such membranes have already been used to observe optomechanical features in an infrared laser diode SM configuration²⁶. A SEM image of the fabricated sample is shown in FIG. 1(a).

The structure is composed of a 300-nm-thick, 300- μm -wide suspended central pad held at each corner by 10- μm -wide tethers anchored at the vertices of a 1-mm-side squared window. Details of the sample fabrication can be found elsewhere²⁶. The membrane pad dimensions were chosen in order to increase the level of OF for SM measurements by creating a reflective surface of size comparable to the focused THz beam spot size ($\sim 250 \mu\text{m}$). To further increase the reflectivity, a 10-nm-thick gold layer was thermally evaporated over the entire membrane surface to produce an almost totally reflective target. The sample was directly glued on the top surface of a piezoelectric ceramic actuator with the fundamental out-of-plane mechanical resonance at $\sim 100 \text{ kHz}$. By exciting the piezo-actuator, the membrane motion was driven and its mechanical response could be investigated. The system composed of the piezo-actuator and membrane sample was mounted inside a vacuum chamber allowing control of the environmental pressure. An initial membrane characterization was performed using a commercial high spatial-resolution

In this letter, we report a significant improvement of

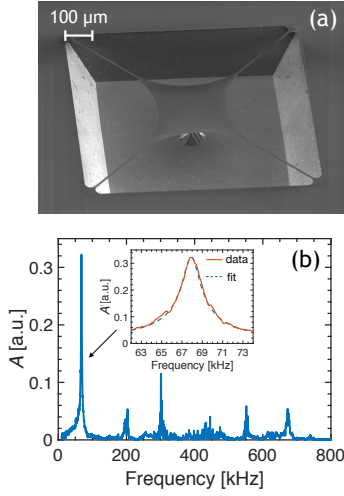


FIG. 1. (a) SEM image of the Si_3N_4 membrane. (b) Membrane mechanical spectrum measured at atmospheric pressure at the membrane center using the LDV. Inset: zoom of the fundamental resonance and corresponding fit (dashed line) using Eq. 2.

LDV (Polytech UHF 120). By applying a flat spectrum voltage excitation to the piezo-actuator, the resonant mechanical modes of the membrane could be observed.

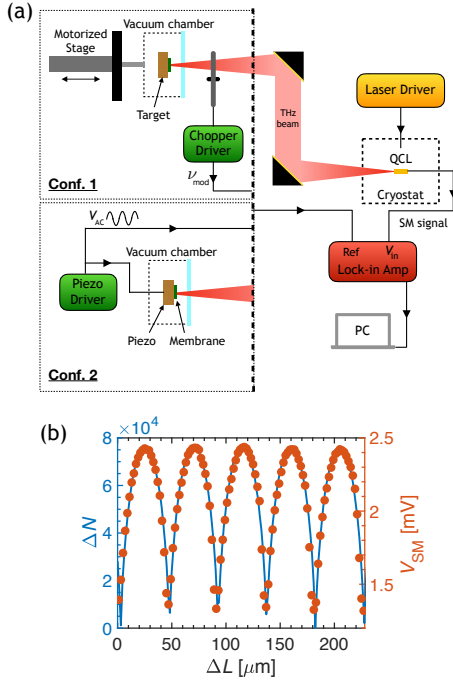


FIG. 2. (a) Sketch of the two configurations of the SM apparatus. (b) Calculated ΔN (blue curve), and measured V_{SM} (red points), as a function of ΔL using configuraton 1.

From the spectrum shown in FIG. 1(b), obtained at atmospheric pressure, the fundamental mechanical mode is observed to be well separated from the higher order modes. Moreover, with the membrane oscillating orthogonally to the

chip-plane, this particular mode ensures that the full THz wavefront reflected from the membrane experiences the same external optical path, thus contributing with the same phase to the SM effect. This makes the fundamental vibrational mode particularly suitable for coherent measurements of membrane vibrations by LFI²⁶and, as such, subsequent measurements here focus on this mode. A complete LDV characterization of the membrane motion as a function of pressure was performed, and is reported for convenience in the Supplementary Material. The data was analysed by modelling the membrane as a one-dimensional driven harmonic oscillator. Defining $A(t)$ and $a(t)$ as the positions of the membrane trampoline and of the tether clamps (moving with the piezo driver) with respect to their common rest positions $A = a = 0$, respectively, the membrane equation of motion can be written as:

$$\ddot{A}(t) + \gamma\dot{A}(t) + \omega_m^2[A(t) - a(t)] = 0 \quad (1)$$

where ω_m is the pressure-dependent membrane resonance angular frequency and γ is the membrane damping coefficient. The oscillation amplitude can be obtained from the imaginary part of the solution, $A(\omega)$, in the frequency domain:

$$\text{Im}[A(\omega)] = \frac{\gamma\omega}{(\omega_m^2 - \omega^2)^2 + (\gamma\omega)^2} \omega_m^2 a_0 \quad (2)$$

where a_0 is the maximum driving oscillation amplitude. By fitting the displacement spectra using Eq. 2, we obtain for each investigated pressure the values of the resonance frequency $\omega_m/2\pi$, the quality factor $Q = \omega_m/\gamma$ and the oscillation amplitude at the resonance frequency A^{max} . As the environmental pressure decreases these three quantities monotonically increase up to a saturation level. The resonance frequency and quality factor change from $\omega_m/2\pi \sim 67.9$ kHz and $Q \sim 40 \pm 2$, respectively, at atmospheric pressure (see inset of FIG. 1(b)) to ~ 73.4 kHz and $\sim 200 \pm 10$ at pressure $\sim 7.3 \times 10^{-3}$ mbar.

A schematic diagram of the experimental apparatus for the THz LFI measurements is presented in FIG. 2(a). We used a THz QCL consisting of a $14\text{-}\mu\text{m}$ -thick GaAs-AlGaAs active region with growth details reported in the literature²⁷. The device was fabricated as a single-metal ridge with longitudinal and transversal dimensions of 1.8 mm and $150 \mu\text{m}$, respectively. The laser was driven in CW mode with a current equal to 510 mA and was maintained at a temperature of 25K using a continuous-flow cryostat. Under these conditions the QCL provided stable single mode emission at 3.34 THz and a large SM response^{15,27}. The THz beam passing through the polythene window of the cryostat was collimated and focused (using two $f/2$ off-axis parabolic reflectors with diameter 50.8 mm) onto the trampoline membrane which constituted the mirror of the external cavity providing OF to the laser. The vacuum chamber containing the membrane was fixed to a motorized stage allowing the external optical cavity length L between the target and the QCL emission facet to be micrometrically changed. The LFI apparatus was used in two configurations. In the first configuration (conf. 1 in FIG. 2(a)), the membrane motion was not excited and the membrane was translated towards the laser facet in $2 \mu\text{m}$ -long steps parallel to the beam propagation direction. The QCL SM voltage V_{SM} was measured by a lock-in amplifier synchronized

to the optical modulation frequency ($\nu_{\text{mod}} = 212$ Hz) imposed to the THz beam by a mechanical chopper placed in front of the vacuum chamber. In the second configuration (conf. 2 in FIG. 2(a)) the membrane equilibrium position was instead kept fixed, but the membrane vibrated at the frequency of the piezo driving excitation, in turn used as the reference of the lock-in amplifier.

To model the SM voltage signal as a function of the target position we used the steady-state solutions of the Lang-Kobayashi equations describing the laser under OF²³. This was done by evaluating the laser emission frequency under OF, ω_F , by numerically solving the so-called excess phase equation:

$$\omega_0 - \omega_F = \frac{k}{\tau_{\text{ext}}} \sqrt{1 + \alpha^2} \sin(\omega_F \tau_{\text{ext}} + \arctan \alpha) \quad (3)$$

where ω_0 is the laser emission frequency without feedback, $\tau_{\text{ext}} = 2L/c$ is the round-trip time in the external cavity, α is Henry's linewidth enhancement factor and k is the OF coupling rate. Using the conventional three mirrors model in the weak feedback regime, where only one reflection from the target is considered, k can be written as $k = \varepsilon \sqrt{\frac{R_{\text{ext}}}{R}} (1 - R)$, in which ε , R and R_{ext} are the coupling-efficiency factor and the reflectivities of the target and laser emission facet, respectively.

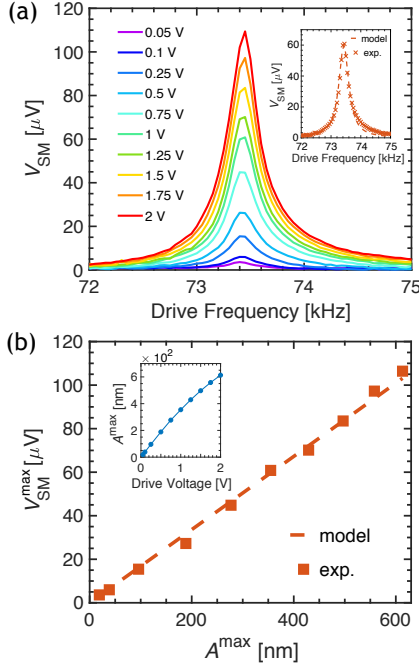


FIG. 3. (a) Measured V_{SM} as a function of the drive frequency for different applied voltages at $P = 0.5$ mbar. Inset: computed (red dashed line) and experimental (red crosses) V_{SM} spectrum with $1V_{\text{RMS}}$ applied to the piezo actuator. (b) Measured (red squares) and calculated (dashed line) $V_{\text{SM}}^{\text{max}}$ as a function of A^{max} . Inset: LDV-measured A^{max} corresponding to the experimental points in the main graph for the same biases and pressure reported in (a).

The parameter ω_F obtained from Eq. 3 determines the laser

carrier number variation ΔN from the threshold carrier number with and without feedback via the following equation:

$$\Delta N = -\frac{2k}{G\tau_c} \cos(\omega_F \tau_{\text{ext}}) \quad (4)$$

where G is the active region modal gain factor and τ_c the laser cavity round-trip time. Starting from the initial external cavity optical length, $L_0 = 47$ cm, ΔN was calculated for each value of L using the best fitting parameters reported in Supplementary Material. The values of ΔN are plotted (blue curve) as a function of the membrane displacement $\Delta L = L_0 - L$ in FIG. 2(b) together with the experimental values V_{SM} (red points) obtained with configuration 1. The theoretical values are in good agreement with the experiment reproducing both the same shape and typical periodicity ($\lambda_F/2$) of the SM signal. From comparison of these curves we obtained the proportionality coefficient β between the calculated ΔN and the measured V_{SM} , found to be 3.1×10^{-8} mV. It should be noted that the calibration factor β depends on the particular value of G , which was fixed as $1.42 \times 10^4 \text{ s}^{-1}$ according to common values in THz QCL literature^{28,29}. Nevertheless, our calibration procedure allows us to correlate experiments and simulations independently of the value assigned to G .

SM measurements of the membrane oscillation amplitude were then performed using configuration 2. V_{SM} measured at an environmental pressure of $P = 0.5$ mbar is reported as a function of the drive frequency and for several RMS drive voltages in FIG. 3(a). Using a Lorentzian spectral line-shape as the fitting function for the data (valid in the experimentally verified high- Q limit), the vibration spectra were observed to have the same resonance frequency $\omega_m/2\pi \sim 73.43 \pm 0.01$ kHz and $Q \sim 198 \pm 2$, independent of the bias applied to the piezo-actuator. These quantities agree with those obtained previously with the LDV. The V_{SM} signal measured in response to the membrane vibrations can be modelled with Eqs. 3-4 for the steady-state solution of the LK model. In fact, with the limit $2\pi/\tau_{\text{ext}} \gg \omega_m$ satisfied, the membrane position at each instant in time can be considered fixed, contributing as a static external optical path for the LK equations. The time-dependent variation of carrier number $\Delta N(t)$ corresponding to a certain membrane oscillation amplitude can thus be numerically obtained by inserting into Eqs. 3-4 the following expression for L :

$$L = L_0 + A(\omega) \cos(\omega_m t) \quad (5)$$

where $A(\omega)$ is the drive frequency-dependent membrane oscillation amplitude (Eq. 2) evaluated using the previously fitted values of γ and ω_m . The total carrier number variation corresponding to the membrane vibration at a given drive frequency, $\Delta N(\omega)$, can then be calculated as the peak-to-peak amplitude of the time-oscillating $\Delta N(t)$. V_{SM} can then be obtained just multiplying $\Delta N(\omega)$ by the previously retrieved β -factor. In the inset of FIG. 3(a), the values of V_{SM} resulting from this model are shown to reproduce well the experimental V_{SM} measured by applying a drive bias of $1V_{\text{RMS}}$ spanning a single frequency at a time in the range 72–75 kHz. For that drive voltage both model and experiment result in a maximum

SM signal of $\sim 61 \pm 1 \mu\text{V}$ obtained for a $A = 355 \pm 5 \text{ nm}$. Only a small deviation between data and model was found on the high-frequency side of the resonance, which we ascribe to a small degree of mechanical anharmonicity of the tethers' motion not included in the model. Both the theoretical and experimental maximum SM voltages, $V_{\text{SM}}^{\text{max}}$, are shown in FIG. 3(b) as a function of the membrane maximum oscillation amplitude, A^{max} . For the experimental points, the reported values of A^{max} are those obtained from the LDV measurements at the same piezo-actuator drive voltage as the SM measurements, and they are shown in the inset as a function of the applied bias. From the main graph it can be observed that the model matches the experimental data and confirms a linear relation between $V_{\text{SM}}^{\text{max}}$ and A^{max} with a slope coefficient of $0.17 \pm 0.01 \mu\text{V}/\text{nm}$. This agreement implies that we are able to detect membrane vibrations with appreciable precision ($\leq 10 \text{ nm}$, limited by the voltage noise of our set-up) down to deeply subwavelength oscillation amplitudes of only a few nanometers. Specifically, the amplitude corresponding to a SM signal $\geq 3 \text{ dB}$ above the voltage noise is $\sim 15 \pm 5 \text{ nm}$.

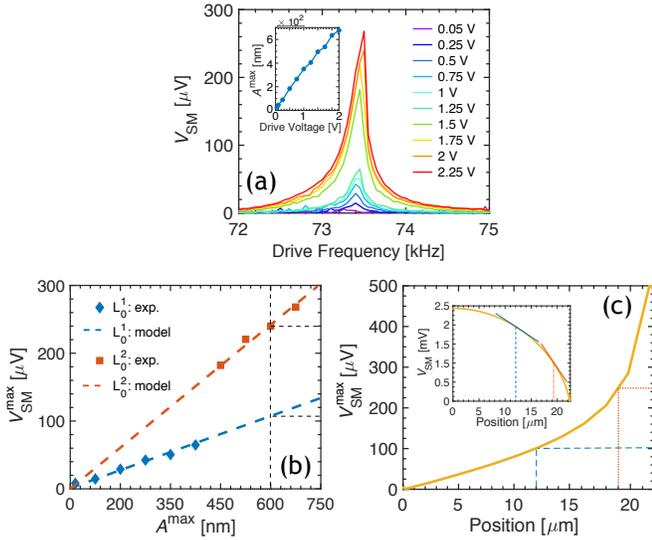


FIG. 4. (a) Measured V_{SM} as a function of the drive frequency for different piezo applied voltages at $P = 4.3 \times 10^{-3} \text{ mbar}$. Inset: LDV measured A^{max} for same piezo drive voltages. (b) Blue diamonds and red squares: experimental $V_{\text{SM}}^{\text{max}}$ obtained from data in (a), as a function of A^{max} obtained for drive voltages until $1.25 V_{\text{RMS}}$ and for the range from 1.5 to $2.25 V_{\text{RMS}}$, respectively. Blue and red dashed lines: calculated $V_{\text{SM}}^{\text{max}}$ for two different membrane positions, labeled L_0^1 and L_0^2 . The vertical dashed line refers to A^{max} considered in the adjacent graph. (c) Calculated $V_{\text{SM}}^{\text{max}}$ for $A = 600 \text{ nm}$ for various equilibrium membrane positions. Blue dashed and red dotted lines indicate the membrane position and $V_{\text{SM}}^{\text{max}}$ corresponding to L_0^1 and L_0^2 , respectively. Inset: calculated *static* V_{SM} in the same range. Vertical dashed and dotted lines represent the same positions. Blue and red solid lines highlight the corresponding different slopes of V_{SM} .

The same SM measurement was also performed at a lower pressure ($P \sim 4.3 \times 10^{-3} \text{ mbar}$). The membrane vibration spectra are shown in FIG. 4(a), while the inset reports the LDV measurements of the maximum membrane displacement

as a function of the drive voltage. Although the maximum amplitudes of the membrane vibrations at $P = 4.3 \times 10^{-3} \text{ mbar}$ do not significantly vary from those at $P = 0.5 \text{ mbar}$, the values of $V_{\text{SM}}^{\text{max}}$ at lower pressure and for drive voltages $> 1.5 V_{\text{RMS}}$ almost double with respect to those obtained at higher pressure. This effect is shown in FIG. 4(b), in which the measured $V_{\text{SM}}^{\text{max}}$ are reported versus the experimental A^{max} as blue diamonds and red squares for drive voltages lower and higher than $1.5 V_{\text{RMS}}$, respectively. From the model it is possible to demonstrate that the two sets of experimental points arise from different external optical lengths, named L_0^1 and L_0^2 . For drive voltages $\leq 1.5 V_{\text{RMS}}$, data are matched by a linear trend with the same slope coefficient as in FIG. 3(b), which results from the model using the membrane distance $L_0 = L_0^1$. For voltages $> 1.5 V_{\text{RMS}}$, the slope increases to $0.39 \pm 0.01 \mu\text{V}/\text{nm}$ corresponding to an external cavity optical length $L_0 = L_0^2 = L_0^1 + 7 \mu\text{m}$. This difference in slope efficiency (or equivalently the SM voltage sensitivity to displacement) can be explained by observing FIG. 4(c) in which the calculated $V_{\text{SM}}^{\text{max}}$ (corresponding to $A^{\text{max}} = 600 \pm 5 \text{ nm}$ for a drive bias of $2 V_{\text{RMS}}$) is plotted (solid curve) against the membrane position. As shown in the inset, the spatial range reported here is a quarter of the SM signal period, i.e. from the top of a fringe, at which the maximum *static* SM signal is measured (Position=0), to the bottom of the same fringe. It can be observed that the SM voltage sensitivity monotonically increases moving away from the position of maximum *static* SM voltage. The lower and higher sensitivities evident in FIG. 4(c) correspond to a distance from the maximum *static* SM voltage of $\sim 12 \mu\text{m}$ and $\sim 19 \mu\text{m}$, respectively, which in turn agree with the corresponding slopes of the *static* SM signal at these positions, highlighted in the inset. In fact, since we were considering displacements $A^{\text{max}} \ll \lambda/2$, the SM voltage sensitivity is expected to be proportional to the derivative of the *static* SM signal. FIG. 4(c) thus reveals that in principle a sensitivity of $\sim 0.83 \pm 0.02 \mu\text{V}/\text{nm}$ can be achieved in our system by fixing $L = L_0 \pm 22 \mu\text{m}$ such that the operating point is close to the minimum of the *static* SM voltage (corresponding to the maximum slope).

In conclusion, we have experimentally demonstrated the detection of deeply subwavelength vibrations ($< \lambda/6000$) by LFI in the THz frequency range and using as an external element a suspended Si_3N_4 membrane. The SM voltage signal arising across the THz QCL active region in response to nanometer oscillations of the membrane was reproduced and uniquely determined by numerically solving the LK model in the steady state regime. The membrane oscillation amplitudes determined from the SM measurements were also found to be in agreement with those measured using a standard laser-Doppler vibrometric technique. The described LFI apparatus can thus constitute a platform for the characterization of the mechanical response of a variety of systems with a precision comparable to that achieved at near-infrared or visible frequencies. Moreover, the proposed system can be employed and implemented for optomechanical applications where the suspended membrane is driven by the radiation pressure; the realization of an optomechanical system constituted by two different lasers coupled through the mechanical motion driven

by radiation pressure represents a promising perspective.

- ¹D. M. Kane and K. A. Shore, *Unlocking dynamical diversity: optical feedback effects on semiconductor lasers* (John Wiley & Sons, 2005).
- ²D. Kleinman and P. Kisliuk, "Discrimination against unwanted orders in the fabry-perot resonator," *Bell System Technical Journal* **41**, 453–462 (1962).
- ³P. King and G. Steward, "Metrology with an optical maser," *New Sci* **17**, 14 (1963).
- ⁴T. Taimre, M. Nikolić, K. Bertling, Y. L. Lim, T. Bosch, and A. D. Rakić, "Laser feedback interferometry: a tutorial on the self-mixing effect for coherent sensing," *Advances in Optics and Photonics* **7**, 570–631 (2015).
- ⁵K. P. G. Robert and S. G. John, "Apparatus for measurement of lengths and of other physical parameters which are capable of altering an optical path length," (1968), uS Patent 3,409,370.
- ⁶P. Nerin, P. Puget, P. Besesty, and G. Chartier, "Self-mixing using a dual-polarisation nd: Yag microchip laser," *Electronics Letters* **33**, 491–492 (1997).
- ⁷A. Seko, Y. Mitsushashi, T. Morikawa, J. Shimada, and K. Sakurai, "Self-quenching in semiconductor lasers and its applications in optical memory readout," *Applied Physics Letters* **27**, 140–141 (1975).
- ⁸T. M. Bosch, N. Servagent, and S. Donati, "Optical feedback interferometry for sensing application," *Optical engineering* **40** (2001).
- ⁹G. Giuliani, M. Norgia, S. Donati, and T. Bosch, "Laser diode self-mixing technique for sensing applications," *Journal of optics A: Pure and applied optics* **4**, S283 (2002).
- ¹⁰S. Donati, G. Giuliani, and S. Merlo, "Laser diode feedback interferometer for measurement of displacements without ambiguity," *IEEE journal of quantum electronics* **31**, 113–119 (1995).
- ¹¹A. D. Rakić, T. Taimre, K. Bertling, Y. L. Lim, P. Dean, D. Indjin, Z. Ikonić, P. Harrison, A. Valavanis, S. P. Khanna, *et al.*, "Swept-frequency feedback interferometry using terahertz frequency qcls: a method for imaging and materials analysis," *Optics express* **21**, 22194–22205 (2013).
- ¹²J. Keeley, J. Freeman, K. Bertling, Y. L. Lim, R. A. Mohandas, T. Taimre, L. H. Li, D. Indjin, A. D. Rakić, E. H. Linfield, *et al.*, "Measurement of the emission spectrum of a semiconductor laser using laser-feedback interferometry," *Scientific reports* **7**, 7236 (2017).
- ¹³P. Dean, A. Valavanis, J. Keeley, K. Bertling, Y. Leng Lim, R. Alhathloul, S. Chowdhury, T. Taimre, L. H. Li, D. Indjin, *et al.*, "Coherent three-dimensional terahertz imaging through self-mixing in a quantum cascade laser," *Applied Physics Letters* **103**, 181112 (2013).
- ¹⁴M. Wienold, T. Hagelschuer, N. Rothbart, L. Schrottke, K. Biermann, H. Grahn, and H.-W. Hübers, "Real-time terahertz imaging through self-mixing in a quantum-cascade laser," *Applied Physics Letters* **109**, 011102 (2016).
- ¹⁵J. Keeley, K. Bertling, P. Rubino, Y. Lim, T. Taimre, X. Qi, I. Kundu, L. Li, D. Indjin, A. Rakic, E. Linfield, A. Davies, and P. Dean, "Detection sensitivity of laser feedback interferometry using a terahertz quantum cascade laser," *Optics Letters* (Accepted).
- ¹⁶P. Dean, Y. L. Lim, A. Valavanis, R. Kliese, M. Nikolić, S. P. Khanna, M. Lachab, D. Indjin, Z. Ikonić, P. Harrison, *et al.*, "Terahertz imaging through self-mixing in a quantum cascade laser," *Optics letters* **36**, 2587–2589 (2011).
- ¹⁷F. Mezzapesa, L. Columbo, M. Brambilla, M. Dabbicco, S. Borri, M. Vitiello, H. Beere, D. Ritchie, and G. Scamarcio, "Intrinsic stability of quantum cascade lasers against optical feedback," *Optics express* **21**, 13748–13757 (2013).
- ¹⁸R. P. Green, J.-H. Xu, L. Mahler, A. Tredicucci, F. Beltram, G. Giuliani, H. E. Beere, and D. A. Ritchie, "Linewidth enhancement factor of terahertz quantum cascade lasers," *Applied Physics Letters* **92**, 071106 (2008).
- ¹⁹P. Dean, A. Valavanis, J. Keeley, K. Bertling, Y. Lim, R. Alhathloul, A. Burnett, L. Li, S. Khanna, D. Indjin, *et al.*, "Terahertz imaging using quantum cascade lasers—a review of systems and applications," *Journal of Physics D: Applied Physics* **47**, 374008 (2014).
- ²⁰Y. Leng Lim, P. Dean, M. Nikolić, R. Kliese, S. P. Khanna, M. Lachab, A. Valavanis, D. Indjin, Z. Ikonić, P. Harrison, *et al.*, "Demonstration of a self-mixing displacement sensor based on terahertz quantum cascade lasers," *Applied Physics Letters* **99**, 081108 (2011).
- ²¹F. Mezzapesa, L. Columbo, M. Dabbicco, M. Brambilla, and G. Scamarcio, "Qcl-based nonlinear sensing of independent targets dynamics," *Optics express* **22**, 5867–5874 (2014).
- ²²F. P. Mezzapesa, L. L. Columbo, G. De Risi, M. Brambilla, M. Dabbicco, V. Spagnolo, and G. Scamarcio, "Nanoscale displacement sensing based on nonlinear frequency mixing in quantum cascade lasers," *IEEE Journal of Selected Topics in Quantum Electronics* **21**, 107–114 (2015).
- ²³R. Lang and K. Kobayashi, "External optical feedback effects on semiconductor injection laser properties," *IEEE journal of Quantum Electronics* **16**, 347–355 (1980).
- ²⁴C. Reinhardt, T. Müller, A. Bourassa, and J. C. Sankey, "Ultralow-noise sin trampoline resonators for sensing and optomechanics," *Physical Review X* **6**, 021001 (2016).
- ²⁵R. A. Norte, J. P. Moura, and S. Gröblacher, "Mechanical resonators for quantum optomechanics experiments at room temperature," *Physical review letters* **116**, 147202 (2016).
- ²⁶L. Baldacci, A. Pitanti, L. Masini, A. Arcangeli, F. Colangelo, D. Navarro-Urrios, and A. Tredicucci, "Thermal noise and optomechanical features in the emission of a membrane-coupled compound cavity laser diode," *Scientific reports* **6**, 31489 (2016).
- ²⁷M. Wienold, L. Schrottke, M. Giehler, R. Hey, W. Anders, and H. Grahn, "Low-voltage terahertz quantum-cascade lasers based on lo-phonon-assisted interminiband transitions," *Electronics letters* **45**, 1030–1031 (2009).
- ²⁸G. Agnew, A. Grier, T. Taimre, Y. L. Lim, K. Bertling, Z. Ikonić, A. Valavanis, P. Dean, J. Cooper, S. P. Khanna, *et al.*, "Model for a pulsed terahertz quantum cascade laser under optical feedback," *Optics express* **24**, 20554–20570 (2016).
- ²⁹A. Hamadou, J.-L. Thobel, and S. Lamari, "Modelling of temperature effects on the characteristics of mid-infrared quantum cascade lasers," *Optics Communications* **281**, 5385–5388 (2008).